Peptide Amphiphiles Hitchhike on Endogenous Biomolecules for Enhanced Cancer Imaging and Therapy

Jared M. Fischer[1,2,], Morgan Stewart[1], Mingchong Dai[1], Samuel Drennan[1], Samantha Holland[3], Arnaud Quentel[1], Sinan Sabuncu[1], Benjamin R. Kingston[1], Isabel Dengos[1], Li Xiang[1], Karla Bonic[1,4], Florian Goncalves[1,4], Xin Yi[1], Srivathsan Ranganathan[1], Bruce P. Branchaud[1], Leslie L. Muldoon[3,5], Ramon F. Barajas Jr[6,7,8], Adem Yildirim[1,4,9,]**

[1]CEDAR, Knight Cancer Institute, School of Medicine, Oregon Health and Science University, Portland, Oregon 97201, United States

[2]Department of Molecular and Medical Genetics, School of Medicine, Oregon Health and Science University, Portland, Oregon 97239, United States

[3]Neuro-Oncology Blood-Brain Barrier Program, Oregon Health and Science University, Portland, Oregon 97239, United States

[4]Department of Biomedical Engineering, School of Medicine, Oregon Health and Science University, Portland, Oregon 97201, United States

[5]Department of Neurology, School of Medicine, Oregon Health and Science University, Portland, Oregon 97239, United States

[6]Advanced Imaging Research Center, Oregon Health and Science University, Portland, Oregon 97239, United States

[7]Department of Radiology, School of Medicine, Oregon Health and Science University, Portland, Oregon 97239, United States

[8]Knight Cancer Institute, School of Medicine, Oregon Health and Science University, Portland, Oregon 97201, United States

[9]Division of Oncological Sciences, Knight Cancer Institute, School of Medicine, Oregon Health and Science University, Portland, Oregon 97201, United States

Abstract

The interactions of nanomaterials with biomolecules in vivo determine their biological fate. Here, we show that a self-assembled peptide amphiphile nanostructure (namely SA-E) dynamically interacts with endogenous biomolecules and takes advantage of naturally occurring processes to target a broad range of solid tumors. Upon in vivo administration, self-assembled nanostructures of SA-E disassemble and reassemble with lipoproteins in circulation. Hitchhiking on lipoproteins prolongs the blood circulation of SA-E and allows it to cross endothelial barriers through transcytosis. At the tumor site, SA-E internalizes into cancer cells by mainly interacting with lipid-raft domains on cell membranes. By exploiting these endogenous interactions, SA-E demonstrated high tumor accumulation with extended retention in various xenograft, syngeneic, patient-derived xenograft, or transgenic mouse and rat models. In addition, SA-E enabled the effective delivery of highly potent chemotherapy to breast and glioma tumors with reduced side effects. With its simple and modular design and universal tumor accumulation mechanism, SA-E represents a promising platform for broad applications in cancer imaging and therapy.

Introduction

Peptide amphiphiles (PAs) spontaneously self-assemble into nanostructures in aqueous solutions through hydrophobic and electrostatic interactions and hydrogen bonding.[1–5] By exploiting the rich chemistry of amino acid side chains and abundant peptide modifications at both the side chains and terminal ends, PA nanostructures with various morphologies have been developed.[6–10] PA nanostructures are naturally biodegradable and biocompatible with low immunogenicity, making them promising delivery platforms for cancer therapy and detection.[11–16] Like any other self-assembled structure, when PA nanostructures are introduced into circulation, they can disassemble as a result of the binding of their amphiphilic building blocks to biomolecules such as albumin or lipoproteins (LPs).[17,18] Thus, the primary focus in the PA research has been to develop new nanostructures with good stability in the blood to allow them to carry payloads to their intended targets.[17–22] While recent studies demonstrated the importance of bio-nano interactions on the biodistribution of nanomaterials, these interactions remained largely unexplored for PA nanostructures.[23–25]

In this work, we explored how PAs interact with blood biomolecules and cells. We revealed a mechanism allowing them to target and enter cancer cells independent of cell state or surface markers. Specifically, we found that weakly interacting PA nanostructures dynamically assemble with endogenous lipoproteins (LPs) in circulation for prolonged blood circulation and tumor microenvironment targeting and then utilize lipid rafts on the cell membranes for cellular entry. LPs are endogenous nanoparticles composed of lipids, cholesterol, and proteins and exhibit several properties that would be expected from an ideal cancer nanomedicine, such as small particle size (~5-80 nm, excluding chylomicrons), prolonged blood circulation with a half-life of up to 5 days, and being non-toxic, non-immunogenic, and biodegradable.[26–30] In addition, LPs can actively cross endothelial barriers through transcytosis,[31,32] enabling their accumulation and retention in solid tumors. Lipid rafts are cell membrane microdomains enriched in lipids, proteins, and cholesterol and over-expressed in cancer cells.[33–36] By exploiting these intrinsic properties of LPs and lipid rafts, weakly interacting PAs target solid tumors without the need for specific targeting strategies.

To study the interactions of PAs with biomolecules, we designed PAs with different charges that self-assemble into spherical or rod-shaped micelles in aqueous solutions, depending on their overall charge. Upon incubation with plasma containing a complex mixture of endogenous

biomolecules, relatively weakly assembled spherical micelles disassembled and reassembled with LPs, while rod-like micelles remained mostly intact. Using a PA that can strongly assemble with LPs (SA-E), we showed that SA-E crosses endothelial barriers via transcytosis only in the presence of LPs. In vitro mechanistic studies showed that SA-E internalizes in cancer cells independent from LPs and their receptors, but instead, it uses lipid rafts for endocytosis. Assembly of SA-E with these endogenous biomolecules enabled its strong tumor accumulation in a broad range of tumor models of breast, colon, pancreatic, brain, skin, prostate, or lung cancers with high tumor-to-background signal ratios. Biodistribution studies showed that SA-E was mostly cleared from normal tissue in 2 days but retained in the tumor for more than 2 weeks. The substantial tumor accumulation and retention of SA-E enabled the detection of early adenomas in transgenic mice and intracerebral glioma tumors in rats. Finally, we showed that when the SA-E is conjugated with a highly potent and toxic chemotherapeutic agent, Monomethyl auristatin E (MMAE), it demonstrated strong antitumor efficacy in aggressive breast and glioma models in mice with reduced side effects compared to the free drug alone.

Results

PA design. The overall design of the PAs used in this study is shown in Fig. 1a. All PAs share a common motif to promote self-assembly through hydrophobic interactions and hydrogen bonding: GGGHAANG with a palmitic acid modification on the N-terminal.[37–39] While keeping this motif the same, we developed 4 PAs with different hydrophilic motifs to generate self-assembled PA structures with different morphologies. In the hydrophilic part, 3 hydrophilic amino acids (glutamic acid, aspartic acid or lysine; E, D, or K, respectively) were used to prepare PAs with negative, positive, or neutral overall charge (Fig. 1a). The PAs were named based on the amino acid in their hydrophilic motif, for instance PAs with E or K in their hydrophilic parts named as SA-E or SA-K, respectively (Fig. 1a). In addition, a cysteine residue was added for dye or drug conjugation. To track the PAs in vivo and investigate the stability of their self-assembled nanostructures in biological solutions, a NIR fluorescent dye (indocyanine green; ICG) was conjugated to the cysteine residue of the peptides through maleimide coupling. All peptide ICG conjugates were purified using high performance liquid chromatography (HPLC), and successful conjugation reaction was verified using liquid chromatography-mass spectrometry (LC-MS) measurements (Supplementary Fig. 1-4).

The morphology of PA self-assemblies dispersed in phosphate buffered saline (PBS, 10 mM, pH 7.4) was investigated using transmission electron microscopy (TEM), which showed that the overall charge determines the morphology of self-assembled PA structures (Fig. 1b). Negatively charged PAs (SA-E and SA-D; net charge of -4) demonstrated a spherical micelle morphology with sizes around 5-10 nm. Positively charged (SA-K, net charge of +2) or neutral (SA-KEK) PAs, on the other hand, formed rod-like micelles with diameters around ~10 nm and lengths reaching several hundred nm.

Stability and interactions of PA structures in blood plasma. To understand the stability of self-assembled PA structures in biologically complex solutions, we utilized human plasma (Fig. 1c). In the absence of plasma, the fluorescence of ICG was quenched in all self-assembled PA structures due to the close packing of ICG molecules.[40,41] Upon the addition of human plasma (10%), an increase in fluorescence intensity was observed preferentially for spherical micelles (SA-E and SA-D) compared to rod-like ones (SA-K and SA-KEK). The fluorescence intensity for SA-E and SA-D continuously increased up to 1 h and reached a maximum at 1 hour. The increase in the ICG fluorescence was significantly lower for SA-K and SA-KEK. These results suggest that while spherical PA micelles quickly disassemble and bind to plasma biomolecules,[42,43] rod-like PA micelles remain mostly self-assembled in human plasma. In addition, we performed molecular dynamic simulations to study the stability of self-assembled structures formed by the PAs. In accordance with experimental results, simulations also suggested more strongly assembled structures for the rod-shaped assemblies; SA-K and SA-KEK (See Supplementary Information for details, Supplementary Fig. 5). Next, we sought to identify the plasma components that spherical PA micelles are interacting with using SA-E because this formulation disassembled rapidly in plasma. The most likely interactions of SA-E in blood are expected to be albumin and LPs, as they are highly abundant and carry lipophilic molecules in circulation.[26–28,44–50] Albumin is the most abundant protein in the blood, representing roughly half of the total circulating proteins.[48] One of the main functions of albumin is to transport endogenous or exogenous hydrophobic molecules. LPs are complex endogenous nanoparticles with shells composed of phospholipids, cholesterol, and apolipoproteins and carrying cholesterol ester and triglycerides in their cores.[28] Based on their density and composition, LPs are divided into four main subgroups: chylomicrons, very low-density lipoproteins (VLDL), low-density lipoproteins (LDL), and high-density lipoproteins (HDL). Similar to albumin, LPs can also transport hydrophobic molecules. Fast protein liquid

chromatography (FPLC) experiments were performed using SA-E in the absence or presence of albumin and LPs. Without albumin or LPs, SA-E eluted from the column as a single narrow peak, as expected for self-assembled micelles with a narrow size distribution of around 10 nm (Fig. 1d). When SA-E was incubated with VLDL, LDL, HDL, or albumin, SA-E was eluted with these LPs or albumin (Supplementary Fig. 6), showing that micelles disassembled and SA-E bound to these biomolecules. To understand if SA-E binds to any LPs or albumin specifically, we then performed FPLC in the presence of all LPs and albumin roughly at their physiological concentrations in 10% human plasma, which showed that SA-E more specifically binds to LPs (Fig. 1d). Only 3.8% of the SA-E was eluted with albumin and the rest of SA-E was eluted with LPs (32.8%, 56.7%, and 6.7% for HDL, LDL, and VLDL respectively), showing the specificity against LPs, especially to HDL and LDL. We also performed FPLC for the SA-E sample incubated in 10% human plasma and observed similar results, although individual peaks of HDL and albumin were not as clear due to the complexity of human plasma and the similar size of HDL and albumin (Supplementary Fig. 7).

To further study the plasma components that SA-E binds, mass spectrometry (MS) was used. For MS experiments, we prepared a biotinylated version of ICG labeled SA-E (SA-Eb, Supplementary Fig. 8). SA-Eb was first incubated in human plasma, then SA-Eb and the plasma components bound to it were pulled down using streptavidin-coated magnetic beads. The eluted protein was analyzed using MS. We also performed pull-down experiments without SA-Eb to detect the proteins that were non-specifically adsorbed to the beads. There were ~2.4-fold more MS counts for the SA-Eb sample compared to only plasma, suggesting that most proteins were specifically pulled down with SA-Eb. For the SA-Eb sample, 28.5% of all detected proteins were apolipoproteins (protein components of LPs), whereas the apolipoprotein content was 11.8% in the plasma only sample (Fig. 1e and Supplementary Table 1). Apolipoprotein B, the main protein component of LDL and VLDL,[51] was non-detectable in the plasma only sample, but it was highly abundant (5.4%) in the presence of SA-Eb. In addition, the concentration of Apolipoprotein A-I, the main protein component of HDL,[51] increased 2.5-fold (18.4% from 7.3%) in the SA-Eb sample. There was only a slight increase in the albumin concentration (33.3% vs. 31.8%), which is in accordance with FPLC results. Overall, these results show that SA-E preferentially assembles with endogenous LPs in the blood compared to albumin.

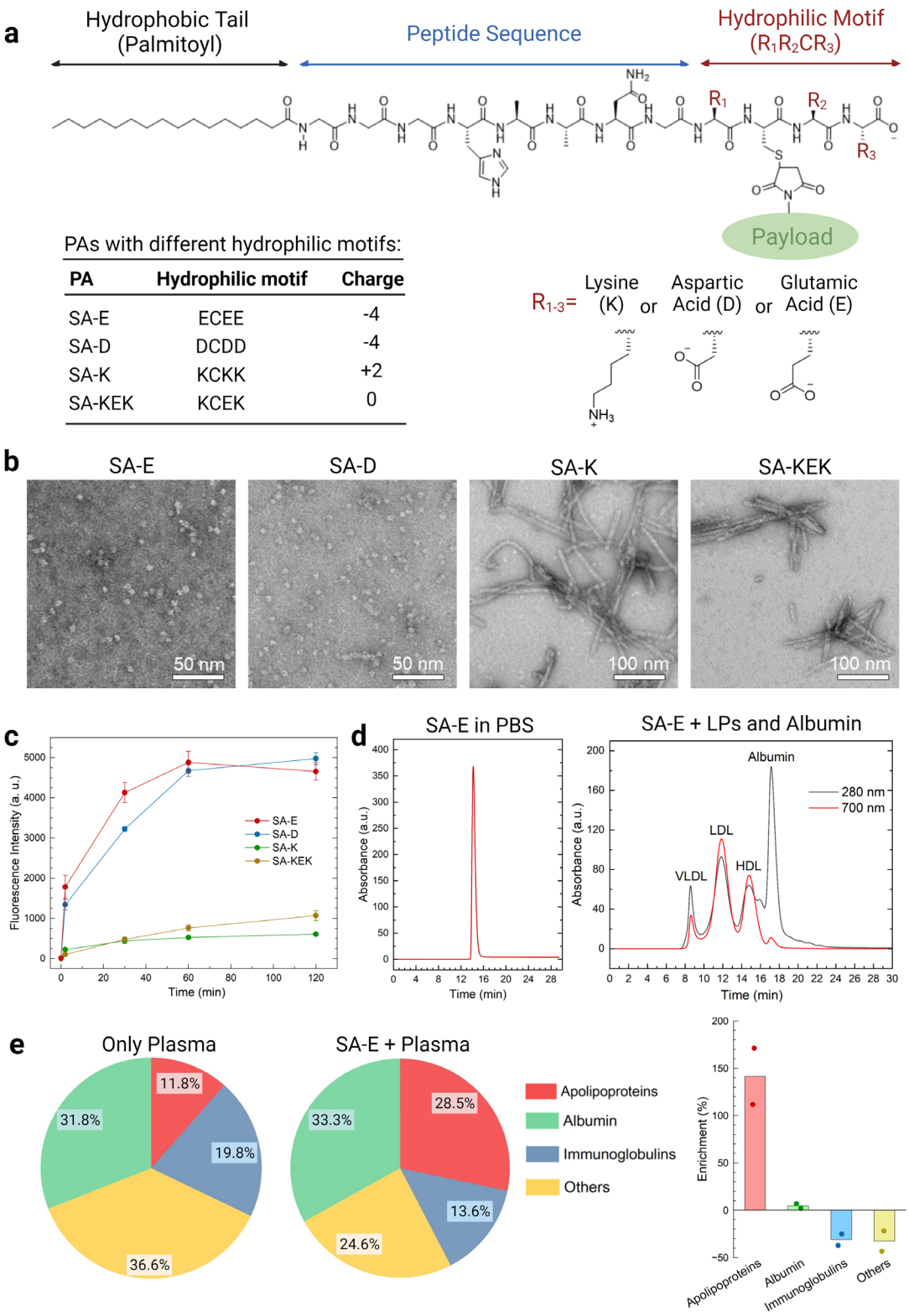
a
Hydrophobic Tail (Palmitoyl)
Peptide Sequence
Hydrophilic Motif ($R_1R_2CR_3$)
Payload
PAs with different hydrophilic motifs:
PA | Hydrophilic motif | Charge
SA-E | ECEE | -4
SA-D | DCDD | -4
SA-K | KCKK | +2
SA-KEK | KCEK | 0
R_{1-3}= Lysine (K) or Aspartic Acid (D) or Glutamic Acid (E)
b
SA-E
SA-D
SA-K
SA-KEK
50 nm
50 nm
100 nm
100 nm
c
Fluorescence Intensity (a. u.)
Time (min)
SA-E
SA-D
SA-K
SA-KEK
d
SA-E in PBS
Absorbance (a.u.)
Time (min)
SA-E + LPs and Albumin
Albumin
LDL
HDL
VLDL
280 nm
700 nm
e
Only Plasma
11.8%
19.8%
36.6%
31.8%
SA-E + Plasma
28.5%
13.6%
24.6%
33.3%
Apolipoproteins
Albumin
Immunoglobulins
Others
Enrichment (%)

Fig. 1. Negatively charged PAs self-assemble into spherical micelles that disassemble in plasma through LP binding. a) Schematic showing the overall molecular structure of the PAs used in this study. Table (bottom left) shows hydrophilic motifs used in different PAs and their overall charge. b) TEM images of PAs showing that negatively charged PAs formed spherical micelles while others formed rod-like micelles. Samples were negatively stained using uranyl acetate. c) Fluorescence intensity of ICG labeled PAs in 10% human plasma over 2 hours. d) FPLC traces of SA-E in PBS or a mixture of LPs and human serum albumin at around their 10% plasma concentrations. Absorbance at 280 nm was used to detect LPs and albumin, and 700 nm was used to detect SA-E. e) Summary of proteins identified in pulled-down proteins in 10% human plasma samples with or without SA-E by mass spectrometry (left panel). Percent enrichment of proteins in the presence of SA-E (right panel). Error bars are standard error of the mean (SEM). Studies were run in triplicates in (c) and duplicates in (e).

SA-E crosses endothelial barriers through LP-enabled transcytosis. Next, we performed in vitro studies to understand the impact of SA-E assembly with LPs on their interactions with endothelial cells. LPs, especially HDL and LDL, can cross endothelial barriers through transcytosis.[31,32,52–54] Thus, we hypothesized that SA-E could also be transcytosed across intact endothelial cell layers by hitchhiking on LPs. To investigate the effect of LP assembly on the transcytosis of SA-E, we utilized human umbilical vein endothelial cells (HUVECs) or BEND3 mouse brain endothelial cells. Endothelial cells were grown on the top layer of transwell plates, and when they formed an intact monolayer at 100% confluence, Cy-3 labeled SA-E (Supplementary Fig. 9) was added into the top well in cell culture media containing human plasma, HDL, or LDL or without any LPs or proteins. To detect transcytosis, Cy3 fluorescence in the bottom compartment was measured at different time points (Fig. 2a). In the presence of human plasma or HDL, a significant transcytosis was observed for SA-E with gradually increasing Cy3 fluorescence intensity over 4 hours for both HUVECs and BEND3 cells. LDL also improved transcytosis in HUVECs to a lower extent but did not in BEND3 cells. In the absence of LPs, the Cy3 fluorescence in the bottom well was negligible for HUVECs, and it was only ~20% of HDL for BEND3 cells, suggesting that LPs, especially HDL, are needed for the transcytosis of SA-E. In addition, the endothelial cell layers were imaged for endocytosed SA-E at the end of the

experiment (Supplementary Fig. 10). Interestingly, independent from the presence of LPs, SA-E was internalized in the endothelial cells. These results suggest that SA-E requires LPs for transcytosis but not for endocytosis.

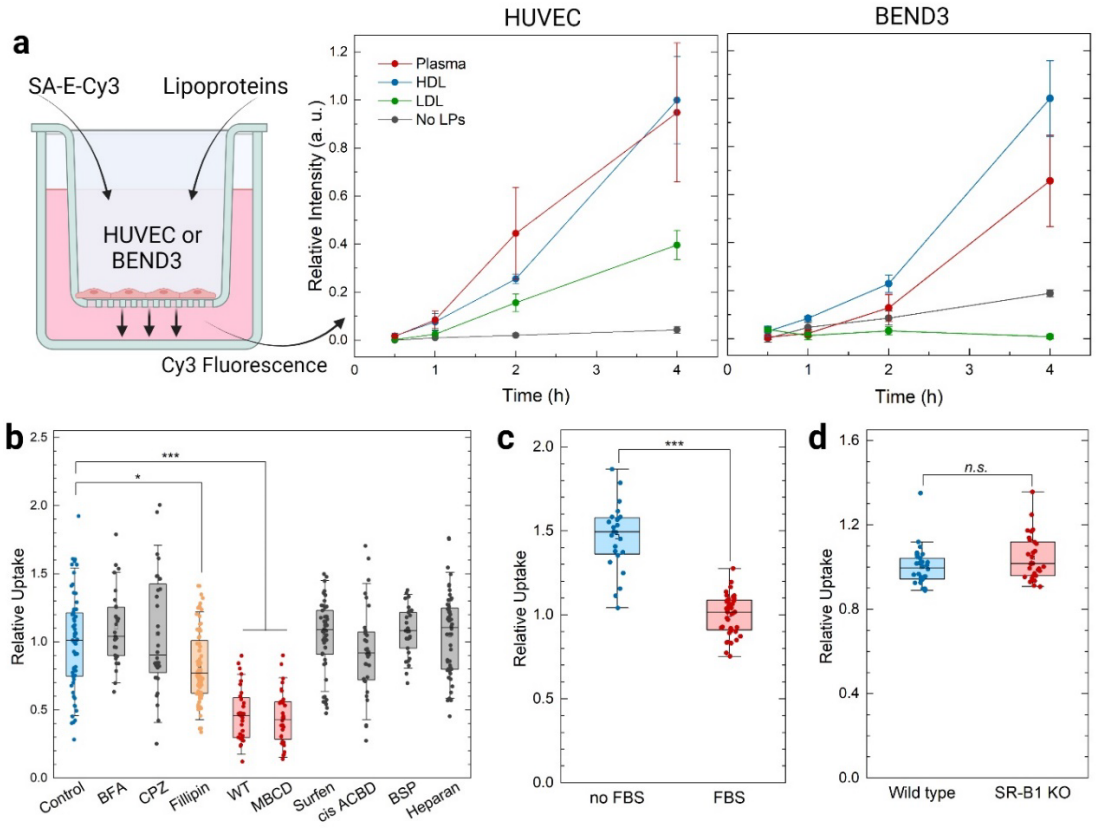

Fig. 2. SA-E utilizes LPs to cross endothelial barriers through transcytosis and lipid rafts for cellular internalization. a) Transcytosis of Cy3 labeled SA-E across an intact layer of HUVECs (left) or BEND3 brain endothelial cells (right) in the presence of human plasma, HDL, LDL, or without any proteins or LPs. Schematic was created with Biorender.com b) Uptake of SA-E by 4T1 cells in the presence of different inhibitors. BFA is Brefeldin A, CPZ is Chlorpromazine, WT is Wortmannin, MBCD is Methyl-b-cyclodextrin, and BSP is Bromosulfalein. c) Cellular uptake of a Cy5 labeled SA-E by 4T1 cells in the presence or absence of FBS. d) Uptake of SA-E by wild type and SR-B1 knock out TRAMP-C2 mouse prostate cells. Error bars are standard error of the mean (SEM) in (a) and standard deviation in (b-d). Studies were run in at least triplicates. Statistical analysis was performed using one-way analysis of variance (ANOVA) in (b) and Student's t test in (c) and (d). *n.s.* is non-significant, *p <0.05 and ***p <0.001.

SA-E utilizes lipid rafts for cellular internalization. We investigated the cellular internalization mechanism of SA-E using 4T1 mouse breast cancer cells and Cy5 labeled SA-E (Supplementary Fig. 11). We used a series of inhibitors to test the different endocytosis pathways (Fig. 2b and Supplementary Fig. 12).[55–57] Wortmannin (WT), a PI3K inhibitor and general inhibitor of endocytosis,[57] significantly decreased SA-E uptake. Methyl-b-cyclodextrin (MBCD), a lipid raft inhibitor,[58] decreased SA-E uptake to a similar extent as Wortmannin. Fillipin, a caveolae-dependent and lipid raft inhibitor,[59] decreased SA-E uptake to a lesser extent. Brefeldin A (BFA) and chlorpromazine (CPZ), both clathrin-dependent inhibitors,[57,60] had no effect on SA-E uptake. Surfen and Heparan both inhibit micropinocytosis by binding to heparan sulfate receptor proteoglycan,[61,62] did not affect SA-E uptake. Since SA-E contains several anionic residues, we used inhibitors of glutamate uptake (cis-ACBD) or organic anionic uptake (bromosulfalein, BSP)[63,64] and found no change in SA-E uptake. These results suggest that SA-E is internalized in cancer cells mainly via lipid raft-mediated endocytosis, which is known to be upregulated in cancer cells,[33,36] and to a lesser extent on caveolae.

Lipid rafts contain a large number of receptors within the raft,[35] including LP-specific receptors such as LDL-receptor (LDL-R) or scavenger receptor class B type 1 (SR-B1),[65-67] therefore, LP receptor-mediated cell entry could still be required. To explore the role of LP receptor-mediated uptake, we first studied the uptake of SA-E by 4T1 cells in the presence or absence of LPs by using cell media with or without fetal bovine serum (FBS). The absence of LPs in cell media did not decrease SA-E uptake. On the contrary, SA-E uptake was ~%60 higher when there were no LPs in the media (Fig. 2c and Supplementary Fig. 13), which suggests a competitive binding of SA-E with LPs and lipid-rafts that can result in the decreased uptake in the presence of LPs. Finally, we studied the impact of SR-B1, a receptor for HDL,[65] on SA-E uptake using an SR-B1 knockout (SR-B1-/-) TRAMP-C2 mouse prostate cancer cell line.[68] Again, we did not observe any change in SA-E uptake between wild-type and knockout isotype controls (Fig. 2d and Supplementary Fig. 14). These results further suggest that cellular uptake is mainly dependent on lipid rafts but independent of specific receptors.

SA-E improved tumor accumulation and retention. Based on the results above, we hypothesized that SA-E can exploit these endogenous biomolecules to specifically target solid tumors by hitchhiking on LPs in circulation for extended blood circulation and transcytosis and

utilizing lipid-rafts for cancer cell internalization. To test this hypothesis, we first studied the tumor accumulation SA-E within a syngeneic mouse 4T1 breast cancer model. ICG conjugated SA-E or free ICG (50 nmole) was intravenously injected into Balb/c mice containing 4T1 tumors in the mammary fat pad. In vivo imaging system (IVIS) imaging showed strong tumor accumulation of SA-E with maximum fluorescence levels detected in tumor at 11 hours post injection (Fig. 3a,b). SA-E signal slowly decreased over 2 weeks with a 50% decrease in the signal ~3 days after injection. SA-E was present in the tumor at detectable levels even after 2 weeks after injection demonstrating its strong accumulation and retention. Background signal was mostly cleared 2 days after injection (Fig. 3a), and tumor to background signal ratio remained above 2.5 from 11 hours to 2 weeks post-injection with a maximum of around 5 from days 2 to 8 (Fig. 3c). Free ICG did not identify the tumor at any time point, and its tumor to background ratio always remained around 1 (Fig. 3a-c).

Pharmacokinetics and safety of SA-E. We examined blood circulation times of ICG conjugated SA-E and free ICG in wild-type mice after intravenous injection (Fig. 3d). SA-E showed prolonged blood circulation with a half-life of ~1 hour. In addition, 10% of the injected dose was still in circulation ~16.4 hours after injection, and it was still detectable 24 hours after injection (~2% of the injected dose), when the experiment was stopped. Free ICG was quickly cleared from the circulation with a half-life in under 5 min, and its concentration decreased below 1% of the injected dose in an hour (Fig. 3d).

Biodistribution of SA-E was investigated in Balb/c mice containing 4T1 tumors in the mammary fat pad. Two days after injection (50 nmole), organs were collected, and SA-E distribution was determined using an IVIS system. Even with tumors <5 mm in size, there was still a ~4-fold higher signal in the tumor compared to the liver and kidney 2 days after administration (Fig. 3e). There was a low ICG signal in the lung and colon, but all other tissues showed no signal above the background. There was a signal in the stool but not in urine, suggesting that SA-E was mainly excreted from the body through bile, as expected for LPs.[69] We also tested different doses of SA-E and found a linear relationship between tumor signal and dose. These results show that SA-E can detect tumors at an injection dose of as low as 8 nmole (Supplementary Fig. 15). Considering the tumor accumulation, retention, and clearance results of SA-E, we selected 2 days as an optimal

imaging time point and 50 nmole as the optimal dose and used these conditions throughout the work unless otherwise stated.

The toxicity of SA-E was studied in wild-type mice. SA-E was injected at a 4-fold higher dose than the optimal imaging dose (200 nmole), and blood samples were collected for toxicity analysis 24 hours after injection. We measured complete blood counts (CBC) for blood toxicity, Aspartate transferase (AST) for liver toxicity, and Creatinine for kidney toxicity. We found no difference between SA-E or sham injection for blood, liver, or kidney toxicity, suggesting SA-E is highly biocompatible (Fig. 3f).

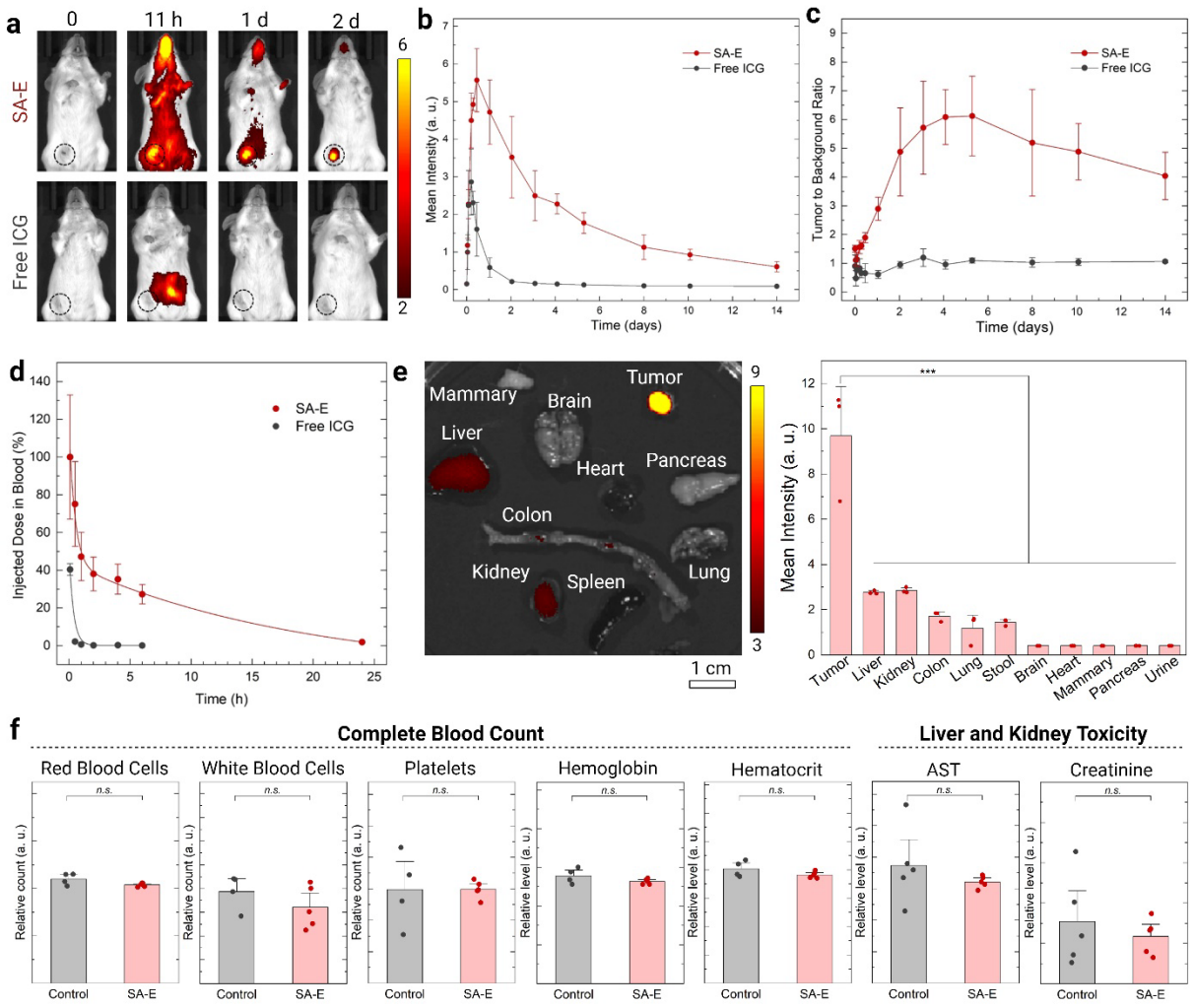

Fig. 3. SA-E shows strong tumor accumulation and retention with excellent biodistribution and no toxicity. a) Representative IVIS images, b) ICG signal in the tumor, and c) tumor to background ratio of intravenously injected free ICG or ICG labeled SA-E (50 nmole) in 4T1

tumor-bearing mice at different time points. Black circles in (a) highlight the tumor location. d) Blood circulation of intravenously injected ICG labeled SA-E or free ICG (50 nmole) in wild type mice. e) Biodistribution of SA-E in 4T1 tumor-bearing mice. IVIS images of the excised organs 2 days after intravenous injection (left) and mean fluorescence intensity of SA-E in tumors and other organs (right). f) Intravenously injected SA-E (200 nmole) showed no toxicity in wild type mice. Blood toxicity counts (left) and liver and kidney toxicity markers (right) did not show any significant change. Control is PBS injected mice. Error bars are standard error of the mean (SEM). Studies were run in at least triplicates. Statistical analysis was performed using one-way analysis of variance (ANOVA) in (e) and Student's t test in (f). *n.s.* is non-significant and ***p <0.001.

SA-E accumulated in a broad range of solid tumors. Since the hypothesized LP hitchhiking mechanism of targeting tumors for SA-E is universal, we tested tumor accumulation in a broad range of cell types and tissue locations. SA-E demonstrated highly specific tumor accumulation in all 10 xenograft, syngeneic, or PDX tumor models of 7 different tissue types (Fig. 4a,b). The tumors used in these studies ranged in size from a few millimeters to a centimeter in syngeneic models in immune competent mice as well as human or rat cells in immunocompromised mice. Also, by utilizing A375 human melanoma cell line expressing luciferase, we showed that the SA-E signal overlapped where the tumor was located. In addition, SA-E demonstrated strong accumulation in 2 transgenic models: MMTV-PyMT and APC^{min}. MMTV-PyMT mice develop early to late cancer lesions in all mammary glands with time.[70] Fig. 4a shows a representative image from a MMTV-PyMT mouse injected with SA-E at 14 weeks of age when one of the mammary glands developed a large tumor (bottom left), and the tumors in other glands were smaller. APC^{min} mice is a transgenic colon cancer model suitable for studying early adenoma lesions.[71] APC^{min} mice were injected with SA-E at 4 months of age when adenomas are known to be present, and the intestines were analyzed 2 days later. Small intestinal adenomas and colon polyps had higher fluorescent signals than the surrounding normal intestine tissue (Fig. 4a). Overlaying the identified tumors with SA-E fluorescence signal revealed that 100% of small intestinal adenomas and colon polyps were positive. In total, 71/71 small intestinal adenomas and 4/4 colon polyps were detected in 3 mice (Supplementary Table 2) by marking all adenomas and polyps using the photograph images. In addition, a good linear correlation between lesion size and

SA-E signal was observed with tumors even smaller than 1 mm^2 being identified (Fig. 4c). These results strongly suggest that SA-E uses a universal mechanism to target a broad range of tumors, including millimeter-sized, early tumor lesions.

Next, we studied the cellular internalization of the SA-E in cancer cells and other cell types in the tumor microenvironment using flow cytometry. SA-E labeled with Cy5 were injected into mice bearing mCherry expressing rat glioma subcutaneous xenografts (RG2), and tumors were harvested 2 days after injection. mCherry cancer cells also containing Cy5 were found ~70% of the time, whereas CD45+ only (white blood cells) or CD45- and mCherry- cells (tumor stroma) contained Cy5 ~35-40% of the time (Supplementary Fig. 16). These results suggest that SA-E is preferentially taken up by cancer cells compared to other cells in the tumor environment.

In vivo tumor accumulation mechanism of SA-E. To confirm the proposed LP hitchhiking based tumor accumulation mechanism of SA-E, we performed in vivo experiments using different knockout strategies. First, Apolipoprotein A-I (ApoAI) knockout mice were used since ApoAI is the major components of HDL; thus, these mice have impaired LP mechanisms.[68] To study tumor accumulation, we used a subcutaneous syngeneic model using mouse MC38 cells. Compared to the tumors formed in wild-type mice, SA-E uptake was significantly lower in ApoAI-/- mice (Fig. 4d), suggesting that assembly with HDL is important for SA-E to accumulate in solid tumors.

Next, we wanted to understand the role of the receptor-mediated uptake in the cancer cells in vivo. We investigated the role of an HDL receptor, SR-B1, for tumor cell uptake in mice. For these studies, we utilized (SR-B1-/-) TRAMP-C2 mouse prostate cancer cells and wild-type cells (SR-B1+/+) as a control.[66] Mice were given both SR-B1-/- and SR-B1+/+ cells subcutaneously on each flank to control for SA-E delivery. Similar to cell culture, SR-B1 was not needed for tumor accumulation (Fig. 4e), suggesting a more universal mechanism of cancer-specific accumulation of SA-E. These results further suggest a mechanism of dynamic assembly to LPs and endothelial escape followed by another dynamic assembly for a non-receptor mediated cancer cell uptake occurs in vivo and is supported by our initial in vitro experiments.

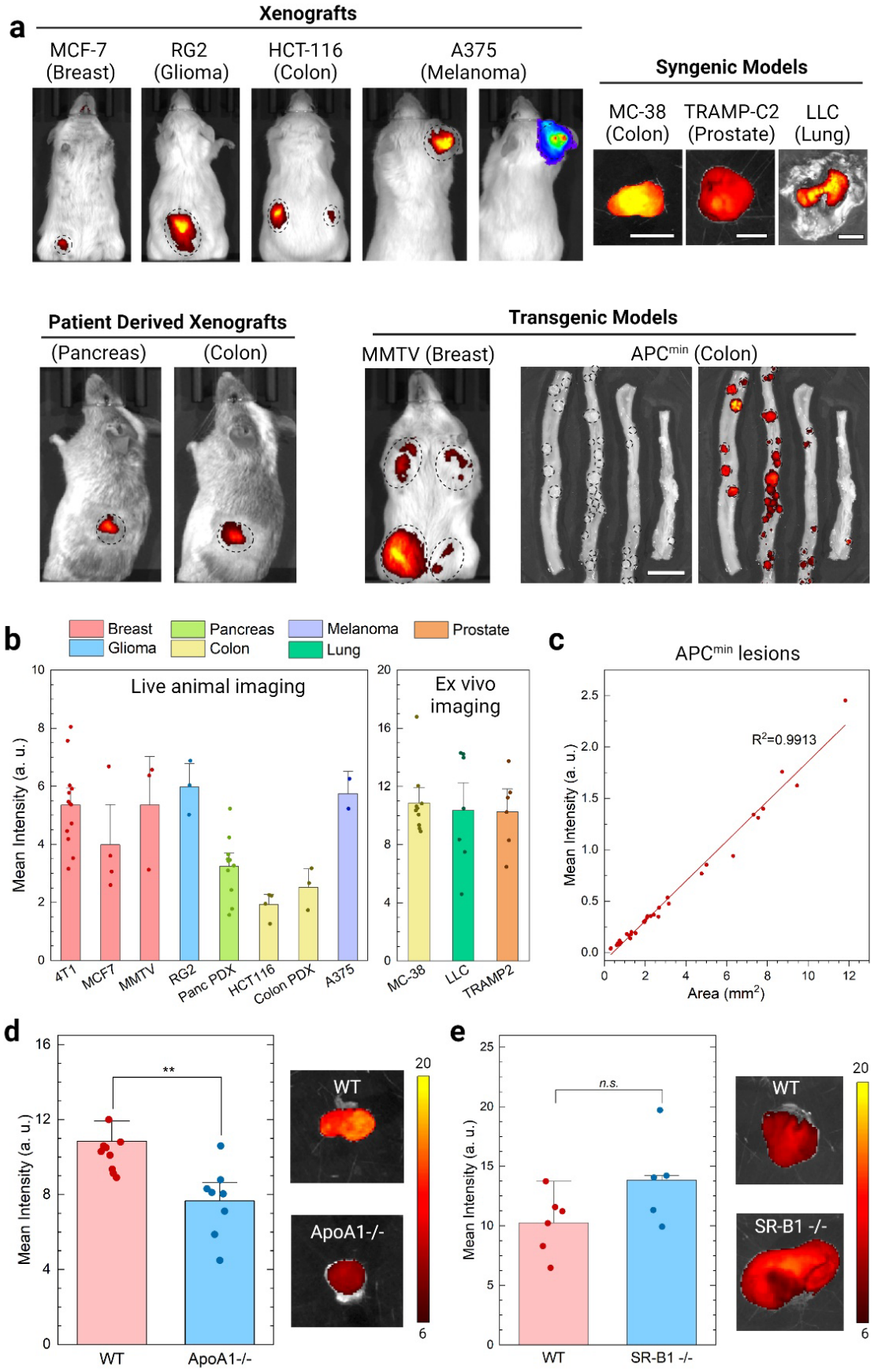
a
Xenografts
MCF-7 (Breast)
RG2 (Glioma)
HCT-116 (Colon)
A375 (Melanoma)
Syngenic Models
MC-38 (Colon)
TRAMP-C2 (Prostate)
LLC (Lung)
Patient Derived Xenografts
(Pancreas)
(Colon)
Transgenic Models
MMTV (Breast)
APCmin (Colon)
b
Breast
Glioma
Pancreas
Colon
Melanoma
Lung
Prostate
Live animal imaging
Ex vivo imaging
Mean Intensity (a. u.)
4T1
MCF7
MMTV
RG2
Panc PDX
HCT116
Colon PDX
A375
MC-38
LLC
TRAMP2
c
APCmin lesions
R2=0.9913
Mean Intensity (a. u.)
Area (mm2)
d
**
Mean Intensity (a. u.)
WT
ApoA1-/-
WT
ApoA1-/-
20
6
e
n.s.
Mean Intensity (a. u.)
WT
SR-B1 -/-
WT
SR-B1 -/-
20
6

Fig. 4. SA-E accumulates in a broad range of solid tumors. a) Representative IVIS images showing the SA-E accumulation in various tumor models of seven different tissues. MCF7, A375, and HCT-116 are human cell lines. RG2 is a rat cell line. MC-38, LLC, TRAMP-C2 are mouse cell lines. In addition, two patient-derived xenografts (PDXs) of human colon and pancreatic cancer were used. MMTV and APC^{min} are a transgenic mouse models of breast and colon cancer, respectively. For MMTV model, mice were injected 14 weeks of age, when all four mammary glands developed tumors with different sizes. For APC^{min} model, bright field (left) and fluorescence (right) IVIS images shows small intestine and colon samples of an APC^{min} mouse injected with SA-E at 4 months of age. IVIS imaging was performed 2 days after ICG labeled SA-E injection (50 nmole) either using live animals or excised tumors. For the luciferase-expressing A375 model, luciferase imaging was also performed (right panel) showing a good overlap between ICG and luciferase signals. Black circles highlight the areas with tumors and adenomas and polyps in APC^{min} model. Scale bars are 1 cm. b) Tumor mean intensity of SA-E in different models: live animal imaging (left) and ex vivo imaging (right). The SA-E intensity in live animals was ~2-fold lower on average than the ex vivo tumors as intact skin and tissue layer covering the tumors in live animals reduces the signal. c) Correlation between lesion size and SA-E signal in the lesions detected in the small intestines and colons of three Apc^{min} mice. d) Mean intensity of SA-E 2 days after injection (50 nmole) into MC-38 tumor-bearing wild type (WT) or ApoA1 knockout mice. Images on the right are representative IVIS images of the tumors. e) Mean intensity of SA-E 2 days after injection (50 nmole) into TRAMP-C2 tumor-bearing mice. Tumors were generated using wild type or SR-B1 knockout cell lines. Images on the right are representative IVIS images of the tumors. Error bars are standard error of the mean (SEM). Studies were run in at least triplicates except the A375 model, which was performed in duplicate. Statistical analysis was performed using Student's t test. *n.s.* is non-significant and $^{**}p < 0.01$.

SA-E accumulated in intracerebral orthotopic rat glioma models. Next, we evaluated SA-E in imaging brain malignancies using two orthotopic glioma models in rats. For these experiments, rat RG2 or human GBM39 cells were injected into the rat cerebrum, and their growth was followed using gadolinium contrast-enhanced magnetic resonance imaging (MRI). When tumors were easily visualized by MRI, we injected ICG labeled SA-E (500 nmole) and imaged the harvested

organs 2 days after injection. Fig. 5a shows the organ distribution of SA-E in an RG2 tumor bearing rat, where a significant ICG fluorescence was observed in the location where the RG2 cells were injected but not in other major organs. To better image the tumors, brains were wholemount dissected through the approximate middle of the tumor in a similar orientation as the MRI. There was near complete overlap between the T1 MRI signal and SA-E signal for both RG2 and GBM39 models (Fig. 5b). Overall, the SA-E signal in the tumor was ~15-fold higher than the adjacent brain tissue for both models (Fig. 5c). The SA-E signal in the tumors was also ~2 and ~5 fold higher than liver and kidney, respectively (Fig. 5c). To confirm specific accumulation of SA-E in glioma cells, we used mCherry expressing RG2 cells. IVIS imaging of a wholemount dissected brain sample showed an almost complete overlap between the mCherry fluorescence of RG2 cells and ICG fluorescence of the SA-E (Fig. 5d). We then froze the brain tissue and took frozen sections and imaged them under a fluorescence microscope. Again, ICG fluorescence overlapped with the mCherry fluorescence, with most cells with mCherry signal also positive for ICG (Fig. 5e). In addition, almost no ICG signal was observed in the brain cells outside tumor. These results further suggest that SA-E can specifically accumulate in cancer cells.

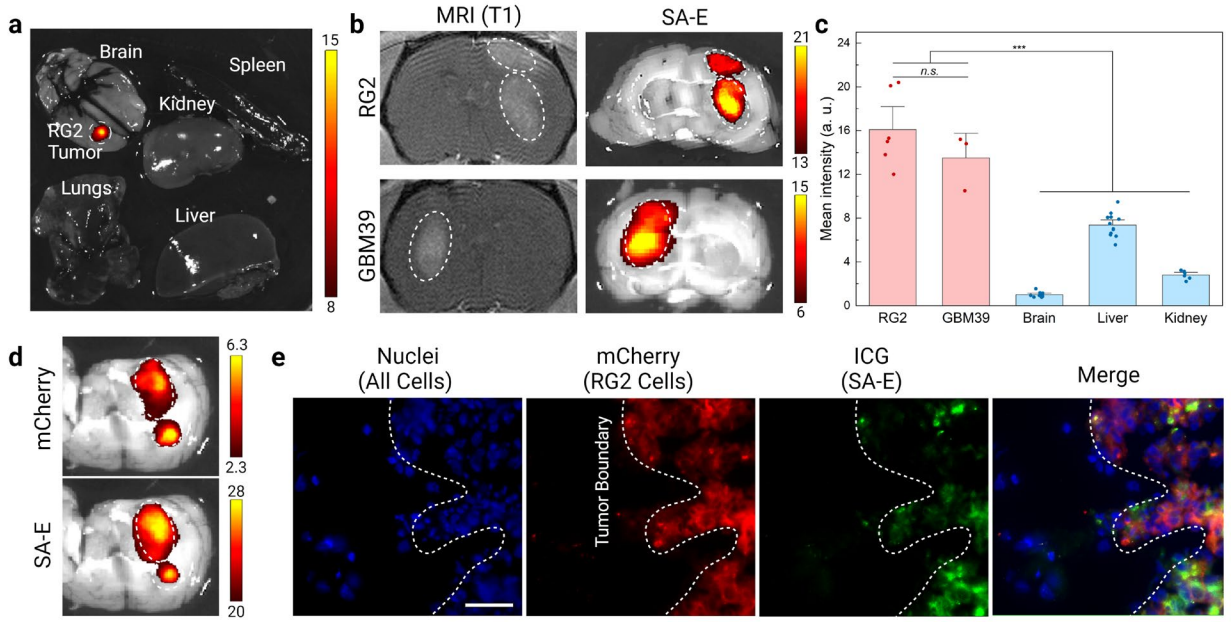

Fig. 5. SA-E demonstrated strong tumor accumulation in intracerebral orthotopic glioma models in rats. a) IVIS imaging of excised organs of a rat bearing a syngeneic RG2 tumor. Organs were harvested 2 days after intravenous injection of ICG labeled SA-E (500 nmole). b) Gadolinium

contrast-enhanced T1 MRI and IVIS imaging of RG2 and PDX GBM39 tumors. MRI imaging was performed shortly before scarifying the rats. IVIS imaging was performed using wholemount dissected brain samples. c) Accumulation of SA-E in RG2 and GBM39 tumors, healthy brain tissue, liver, and kidney in rats. d) IVIS imaging mCherry expressing RG2 tumor sections showing a good overlap between the mCherry signal of RG2 and the ICG signal of SA-E. e) Fluorescence microscope images of a brain tissue section with mCherry expressing RG2 tumors. Scale bar is 100 μm. Error bars in (c) are standard error of the mean (SEM). Studies were run in at least triplicates. Statistical analysis was performed using one-way analysis of variance (ANOVA). *n.s.* is non-significant, and ***p <0.001.

SA-E enables more efficient and safer chemotherapy. Based on strong tumor accumulation and retention of SA-E, we hypothesized that SA-E can improve the efficacy of chemotherapies and decrease their side effects. To evaluate SA-E in drug delivery to solid tumors, we conjugated Monomethyl auristatin E (MMAE), which is a highly potent tubulin inhibitor.[72,73] A commercially available MMAE prodrug (vcMMAE)[73] with a Cathepsin B cleavable linker was conjugated to SA-E through maleimide thiol coupling and purified using HPLC (Supplementary Fig. 17). Cytotoxicity of SA-E-MMAE was first tested in vitro using 4T1 and RG2 cells. Compared to free MMAE, SA-E-MMAE showed ~140 and ~150 fold less toxicity against 4T1 and RG2 cells with an IC50 values of 1.18 μM and 0.21 μM, respectively (Supplementary Fig. 18). A decrease in the cytotoxicity for prodrugs can be expected as these drugs need be activated by enzymes or pH first. Also, RG2 cells were more sensitive to MMAE than 4T1 cells with ~5.5-fold lower IC50 values for both free MMAE and SA-E-MMAE.

We then tested SA-E-MMAE in the 4T1 orthotopic mouse model. 4T1 cells were injected into the mouse mammary fat pad of wild-type mice. 2 days after injection, mice were intravenously injected with free MMAE (0.1 or 0.3 mg/kg), SA-MMAE (0.3 or 0.6 mg/kg), or PBS over 11 days. Free MMAE injections resulted in a slight reduction in tumor growth (Fig. 6a). While free MMAE was tolerated at 0.1 mg/kg, increasing the dose to 0.3 mg/kg resulted in high toxicity with rapid weight loss, and treatment needed to be stopped after the third injection (Fig. 6b). SA-E-MMAE was tolerated much better at higher doses. There was not any significant weight loss at a 2-fold higher dose of 0.6 mg/kg with SA-E-MMAE. Importantly, SA-E-MMAE showed significantly

reduced tumor growth compared to both free MMAE and PBS control tumors (Fig. 6a). While there was not any reduction in the tumor growth rate at the dose of 0.3 mg/kg, increasing the dose to 0.6 mg/kg resulted in around 75% reduction in the tumor volume, without any significant body weight loss. Finally, we tested the antitumor efficacy of SA-E-MMAE against RG2 xenografts in nude mice. For these experiments, we further increased the SA-E-MMAE dose to 1 mg/kg. Similar to 4T1 results, we observed a significant reduction in the tumor volume, around 80%, compared to the control (Fig. 6c). While a slight weight loss observed at the beginning of the therapy, overall the mice tolerated 5 doses of SA-E-MMAE injections at 1 mg/kg (Fig. 6d). These results suggest that SA-E can be conjugated to chemotherapy for improving the therapeutic index of chemotherapies to improve their antitumor activity with reduced side-effects.

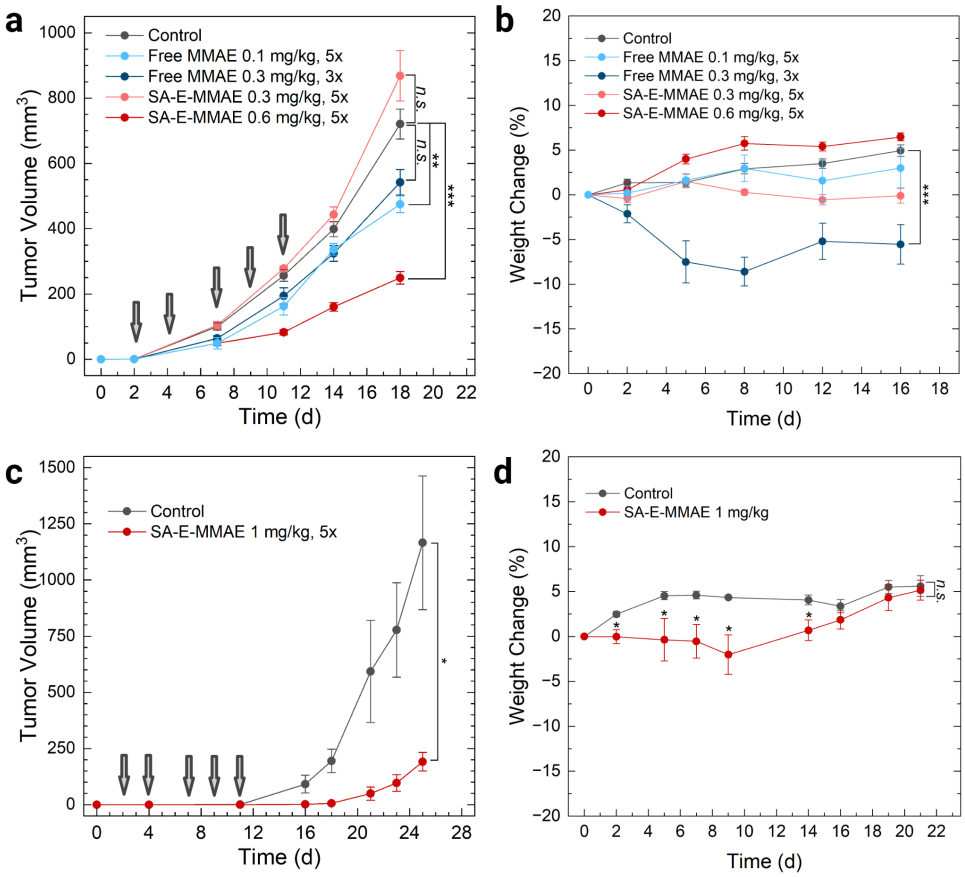

Fig. 6. SA-E improves the antitumor efficacy and safety of MMAE. a) Tumor volume of 4T1 tumor bearing mice received PBS (n=18), 0.1 mg/kg of free MMAE (n=3), 0.3 mg/kg of free MMAE (n=5), 0.3 mg/kg of SA-E-MMAE (n=5), or 0.6 mg/kg of SA-E-MMAE (n=5). All mice received 5 doses of PBS, free MMAE, or SA-E-MMAE except 0.3 mg/kg free MMAE group,

which received first 3 doses due to significant weight loss. b) Average body weight change of the mice that received the treatments in (a). c) Tumor volume of RG2 tumor bearing mice received 5 doses of intravenous injection of PBS (n=4) or 1 mg/kg of SA-E-MMAE (n=4). d) Average body weight change of the mice that received the treatments in (d). Grey arrows in (a) and (c) show the days that the mice received PBS or drug injections. Statistical analysis was performed using two-way analysis of variance (ANOVA) in (a) and (b) and Student's t-test in (c) and (d). *n.s.* is non-significant, $*p < 0.05$, $**p < 0.01$, and $***p < 0.001$.

Discussion

Overall, our rationally engineered peptide amphiphile SA-E showed strong tumor accumulation utilizing LP hitchhiking and lipid raft mediated cellular entry to enhance delivery to solid tumors. Fig. 7 summarizes the proposed mechanism of SA-E for improved tumor accumulation based on the results that we obtained in this study. In circulation, SA-E quickly disassembles and preferentially binds to LPs (Fig. 1). LP binding significantly prolongs blood circulation of SA-E (Fig. 3d), allowing them to pass the tumor site numerous times to accumulate more efficiently. When LP-SA-E assemblies reach the tumor site, first, they need to cross the endothelial barrier to accumulate in the tumor. As endogenous nanoparticles, LPs are transcytosed across vascular barriers.[31,32,52] In fact, our results showed that LPs were important for the transcytosis of SA-E (Fig. 2a). Finally, in the tumor site, they can internalize into cancer mainly through binding to lipid rafts (Fig. 2b-d).

LPs are endogenous non-toxic, non-immunogenic, biodegradable, naturally tumor targeting nanoparticles with sizes down to 5 nm.[26] As a result of these attractive properties, LPs have been exploited to develop nanomedicine platforms for the detection and therapy of cancer.[28,66] These studies have typically used purified or reconstituted LDL or HDL as nanocarriers for the intended imaging or therapy application.[26,74] Efforts also have been devoted to developing lipoprotein mimetic nanoparticles by mixing phospholipids, cholesterol, and apolipoproteins.[28,75] While these studies showed promise in preclinical studies, their clinical translation was hampered by the challenges in the reproducible and large-scale production of either purified or reconstituted LPs or their mimetics.[26] SA-E overcomes the limitations of current LP-based cancer theranostic approaches by forming complexes with endogenously circulating LPs. SA-E conjugated with ICG

or another small molecule such as MMAE can be reproducibly prepared at a large scale. It is challenging to apply a LP hitchhiking approach for the delivery of most chemotherapies as they are usually already hydrophobic molecules, and lipid modification will further increase their hydrophobicity. Increasing their hydrophobicity can result in poor drug pharmacokinetics, preventing them from reaching a therapeutic concentration within the tumor.[76] Thus, applying this strategy for delivering cargos to solid tumors remained rare and limited with more hydrophilic drugs such as Gemcitabine.[77–80] In our approach, the peptide backbone of SA-E addresses this limitation by improving the solubility of SA-E conjugated with contrast agents or drugs while still providing the benefits of lipoprotein binding.

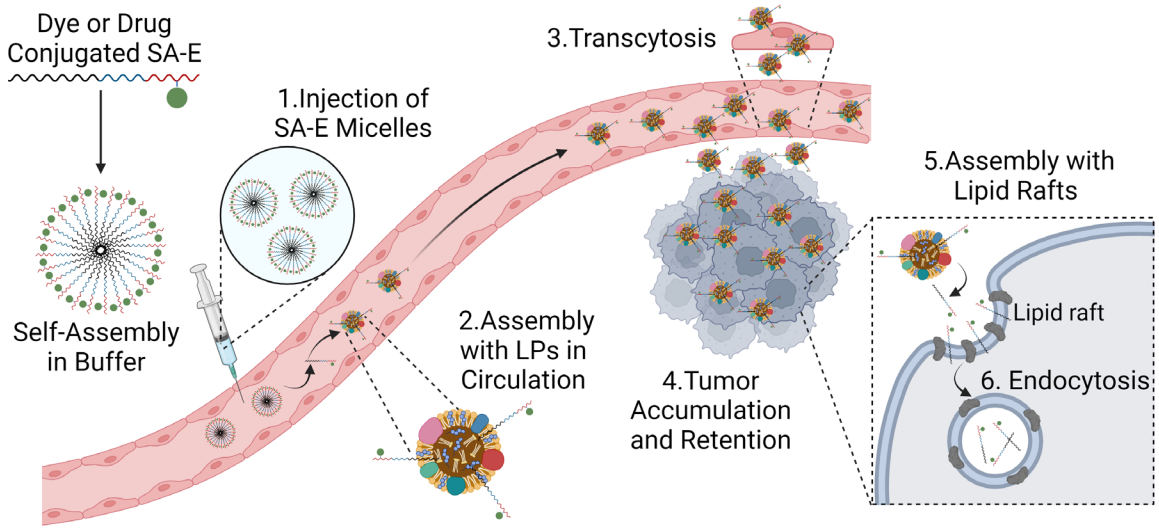

Fig. 7. Schematic showing the proposed tumor accumulation and cancer cell internalization mechanisms of SA-E. Created with Biorender.com.

In summary, we present a new mechanism for weakly assembled PA nanostructures to specifically accumulate in a broad range of cancers based on their in-situ assembly with LPs in circulation and lipid rafts in the tumor microenvironment to facilitate delivery to solid tumors. We demonstrated the high accumulation of our PA, SA-E, in various mouse and rat models, including transgenic models, patient-derived xenografts, orthotopic glioma tumors, and early lesions. In addition, we showed that SA-E can improve the efficacy of a chemotherapy drug with reduced side effects. The

findings of this study underscore the importance of interactions of nanomaterials with biomolecules on their fate in vivo and represent a novel way of exploiting these interactions to develop platforms with universal cancer-targeting ability.

Methods

Materials. Peptides were commercially obtained from Genscript with purity >95%. The following reagents were used: ICG maleimide (Iris Biotech, RL-2820), ICG (Fisher Scientific, I0535100MG), Cy5 maleimide (BroadPharm, BP-22552), Cy3 maleimide (Lumiprobe, 21080), vcMMAE (MedChem Express, HY-15575), MMAE (MedChem Express, HY-15162), HDL from human plasma (Sigma-Aldrich, SAE0054), LDL from human plasma (Sigma-Aldrich, SAE0053), VLDL from human plasma (Millipore Sigma, 437647), human serum albumin (Fisher Scientific, OSRHSA10), pooled human plasma (Innovative Research, IPLAWBK2E50ML), brefeldin A (Alfa Aesar, J62340), bromsulphalein (MedChem Express, HY-D0217), chlorpromazine hydrochloride (Sigma-Aldrich, C8138), cis-ACBD (Tochris, 0271), fillipin (Sigma-Aldrich, F9765), heparin sodium salt (Sigma-Aldrich, H3149-10KU), methyl-β-cyclodextrin (Sigma-Aldrich, C4555-5G), surfen dihydrochloride (MedChem Express, HY-122704A), and wortmannin (Alfa Aesar, J63983), bovine serum albumin (VWR, 0332), 4',6-diamidino-2-phenylindole (DAPI) (Sigma-Aldrich, D9542), Hoechst stain (Invitrogen, H3570), 3-(4,5-dimethylthiazol-2-yl)-2,5-diphenyltetrazolium bromide (MTS) cell proliferation assay (Abcam, ab197010). Gadodiamide (GdDTPA-BMA, Omniscan®, GE Healthcare Inc. Marlborough, MA) MRI contrast was purchased through the OHSU in-patient pharmacy. Manufacturers and catalog numbers of additional materials such as antibodies are given in the text below.

Preparation PA dye or drug conjugates. 4 mg of SA-E (2.92 μmol) and 3.21 μmol (1.1 eq) of maleimide-functionalized dyes or drugs were mixed in 2 mL of anhydrous DMSO (Sigma Aldrich, 900645). The mixture was incubated at room temperature overnight under gentle shaking (300 rpm). Same protocol was used to conjugate ICG to other PAs (SA-D, SA-K, SA-KEK, and SA-Eb). The progression of the reaction was tracked using LC-MS, employing an Acquity UPLC system (Waters) equipped with a SQ Detector 2 (Waters) and a reverse-phase column (Waters, ACQUITY UPLC BEH C18 Column, 130Å, 1.7 μm, 2.1 mm x 50 mm). A solvent gradient from water/acetonitrile (95:5) with 0.1% formic acid to water/acetonitrile (5:95) was run over 9 minutes

at a rate of 0.4 mL/min. Then, purification of the reaction mixtures was conducted using HPLC (Waters 1525, binary HPLC pump) with a reverse-phase column (Waters, XBridge BEH C18 OBD Prep Column, 130Å, 5 μm, 19 mm x 150 mm). The solvent gradient in the HPLC method was gradually adjusted from water/acetonitrile (95:5) to (5:95) with 0.1% trifluoroacetic acid over a 45-minute run at a flow rate of 0.8 mL/min. A UV/Visible detector (Waters 2489) was applied to monitor the absorbance of eluents at 230 nm. The solutions collected from the HPLC runs were concentrated and lyophilized. Finally, purified conjugates were dissolved in sterile PBS (10 mM, pH 7.4) at concentrations between 1-2.5 mM and stored at -20 °C.

TEM imaging of PA nanostructures. For TEM imaging, PA conjugated with ICG were dissolved in ultrapure water at a concentration of 200 μM. Then, PA solutions (5 μL) were placed on carbonfilm 200 copper mesh TEM grids, incubated for 5 min before blotting, and air dried. For negative staining of the samples, a 2% uranyl acetate solution was prepared in ultrapure water and filtered using a 0.1 μm syringe filter. 20 μL of filtered uranyl acetate solution was then placed on a Parafilm piece and TEM grids were floated on this droplet for 7 min. Finally, TEM grids were blotted to remove excess stain and dried at room temperature. TEM imaging was performed using a Tecnai microscope (FEI).

Stability of PA nanostructures in plasma. ICG conjugated PAs were dissolved in PBS (10 mM, pH 7.4) at a concentration of 100 μM and 90 μL aliquots of these solutions were added to a 96 well plate (4 wells for each PA). Then, 10 μL of pooled human plasma was added to each well and fluorescence spectra of ICG was recorded using a microplate reader (TECAN Spark 20M) at different time points. Plate was incubated at 37 °C between measurements.

FPLC experiments. All FPLC experiments were performed using SA-E conjugated with ICG at a final concentration of 250 μM in filtered PBS (10 mM, pH 7.4). For analysis of SA-E interaction with purified LPs, VLDL, LDL, HDL, and human serum albumin were diluted in filtered PBS to approximate concentrations found in 10% human plasma; 0.0025 mg/mL, 0.13 mg/mL, 0.05 mg/mL, and 5 mg/mL respectively. SA-E was incubated with the purified LP/protein mixture for 30 min at 37 °C prior to injection. For analysis of SA-E interaction with plasma, SA-E was incubated in PBS containing 10% pooled human plasma for 30 min at 37 °C prior to injection. Total volume injected for all samples was 400 μL. All data was collected on an ÄKTA pure™ chromatography system using the following running conditions: size exclusion chromatography

on a Superose 5 Increase 10/300 GL column with a column volume (CV) of 30 mL, pre-column pressure limit of 5 MPa, delta-column pressure limit of 2.6 MPa, flow rate of 0.75 mL/min, in 100% PBS. Sample running method included first an equilibration step prior to injection of sample with 100% PBS for 0.5 CV, followed by sample application via 1 mL capillary loop in 100% PBS, and finished with a linear elution consisting of 2 CV collected in 1 mL fractions. The UV-Vis detector wavelengths used to detect eluting proteins were 214 nm, and 700 nm to detect all proteins/lipids and SA-E, respectively.

Mass Spectrometry. Samples were prepared for mass spectrometry analysis via a pull-down of a biotinylated version of the SA-E probe (SA-Eb, 100 μM) incubated with 50% pooled human plasma at 37 °C for 2 hours. Prior to incubation with the SA-Eb-plasma mixture, magnetic streptavidin-coated beads (Dynabeads MyOne Streptavidin T1, Invitrogen, 65601) were washed with PBS (10 mM, pH 7.4) then blocked with 1% casein equal to the total initial volume of beads for 15 min at room temperature. After blocking, beads were washed again with PBS. Beads were then combined with SA-Eb-plasma solution, 25 μL beads to 200 μL mixture. This mixture was then incubated at room temperature for 30 min. After incubation, remaining solution was removed and beads were washed five times with PBS. Bound SA-Eb were eluted from beads in 30 μL 0.5% Triton X-100 solution. For plasma control, the incubation with SA-Eb step was skipped, and 50% plasma in PBS was incubated with beads and washed and eluted in the same method as the SA-Eb-plasma solution. The elution solutions were then analyzed by the Proteomics Shared Resource facility at Oregon Health & Science University (See Supplementary Information for details).

Cell lines. Cell lines used for the experiments were all tested for Mycoplasma at least once every other year. Following cell lines were used: HUVEC (Human umbilical vein endothelial cells, ATCC #PCS-100-013), Bend3 (mouse brain endothelial cells, ATCC #CRL-2299), HCT116 (human colorectal cancer, ATCC CCL-247), A375-Luc/iRFP (human melanoma, Creative Biogene CSC-RR0254), MCF7 (human breast cancer, ATCC HTB-22), 4T1 (mouse breast cancer, ATCC CRL-2539), RG2 (rat glioma, ATCC CRL-2433), and LL/2 (mouse lung cancer (LLC1), ATCC CRL-1642). MC38 mouse intestinal epithelial cancer cells were provided by Dr. Melissa Wong at OHSU. TRAMP-C2-SR-B1+/+ and TRAMP-C2-SR-B1-/- mouse prostate cancer cells were provided by Jonathan D. Smith at Case Western Reserve University. Human derived PDX39 glioblastoma cells were provided by Dr. Jann N. Sarkaria at Mayo Clinic. Patient derived

pancreatic or colon cancer cells were obtained at OHSU with patient consent and cultured for at least 5 passages. Cell lines were maintained in either RPMI Medium 1640 (Gibco, 11875093) supplemented with 10% fetal bovine serum (FBS) (Cytiva, SH30396-03) and 5% penicillin-streptomycin (pen-strep) (Gibco, 15140163) or DMEM with 4.5 g/L D-glucose, L-glutamine, and 110 mg/L sodium pyruvate (Gibco, 11995065) and supplemented with 10% FBS and 5% pen-strep as the growth media in the incubator at 5% CO_2. For mCherry transfection of RG2 cells, lentivirus targeting mCherry to the cell membrane (Takara, 0026VCT, rLV.EF1.mCherry-Mem-9) was used according to manufactures recommendation. Transfected cells were passaged at least 10 times before being used for in vivo experiments.

Transcytosis experiments. HUVEC or Bend3 cells were seeded onto 24 well plate transwell membranes at 4×10^4 cells per transwell insert in 100 µL of respective media (Vascular cell basal medium (ATCC #PCS-100-030) with endothelial cell growth kit – VEGF (ATCC #PCS-100-04) for HUVEC, DMEM (ATCC #30-2002) with 10% FBS for Bend3). The remainder of the well was filled with 0.6 mL of media. Cells were left to grow for 96 hours with fresh media every 24 hours to achieve a consistent and mature endothelial cell monolayer. Once an intact layer of endothelial cells is formed, SA-E labelled with Cy3 was added to a final concentration of 75 µM to endothelial cell media with or without HDL (0.7 mg/mL), LDL (0.7 mg/mL), or Human plasma (10%). The transwell system was incubated at 37 °C and at 30 min, 1 hour, 2 hours and 4 hours, 100 µL was removed from the lower chamber and immediately replaced with 100 µL of fresh endothelial cell media. Cy3 fluorescence of the lower chamber solutions was measured with an excitation at 555 nm, emission at 575 nm with a band width of 5 nm using a microplate reader (TECAN Spark 20M).

To image the endothelial cells on the transwell membrane they were washed twice with PBS (10 mM, pH 7.4), fixed for 15 min at room temperature with 4% paraformaldehyde, and rinsed twice with PBS. Immunofluorescence staining was done by adding 100 µL of PBS with 0.1% Triton-X 100 to permeabilize the cells. Anti-VE-cadherin antibody (Abcam, ab33168) was then added at a 1:200 dilution in PBS, 1% BSA, 0.1% Triton-X 100 and 0.01% sodium azide and incubated for 2 hours at room temperature. The membrane was then washed three times, for 5 min with PBS at room temperature. Goat anti-rabbit Alexa Fluor 647 (Jackson ImmunoResearch, 111-605-144) was added at a 1:400 dilution along with DAPI at 0.5 µg/mL in PBS, 1% BSA, 0.1% Triton-X 100

and 0.01% sodium azide for 30 min at room temperature. The membrane was washed twice with PBS for 5 min at room temperature. The membrane was then cut out using a scalpel and placed on a standard glass slide and mounted with Vectashield antifade mounting media (Fisher Scientific, NC9265087) with a cover slip placed on top. Imaging was done on the Lecia Thunder Epifluorescence microscope with a 20X objective (Leica microsystems HC PL APO 20x NA:0.80) with standard excitation and emission filters.

Cellular uptake. To explore the effect of serum proteins and different inhibitors on the cellular uptake of SA-E, 2-4×10^4 4T1 cells were added to each well and were grown to near confluency (1-2 days) in 96 well plates with black walls and flat glass bottom. For cellular uptake mechanism studies, the growth media (RPMI containing 10% FBS) was exchanged for 100 µL of FBS free media, then returned to the incubator. Inhibitors (brefeldin A, bromsulphalein, chlorpromazine hydrochloride, cis-ACBD, fillipin, heparan, methyl-β-cyclodextrin, or wortmannin) were made in FBS free media at a concentration of 1 mM. Then, 1 µL of media containing inhibitors was added to wells, so that the final drug concentration in each well was 10 µM. The plate was returned to the incubator for 20 min. After incubation, Cy5 conjugated SA-E was added to all wells such that the final concentration was 20 µM per well. The plate was returned to the incubator for 30 min. After which all wells were aspirated, washed 3 times with 150 µL of sterile PBS (10 mM, pH 7.4), 100 µL of FBS free media was added, and returned to the incubator for 1 hour. Finally, Hoechst staining and fluorescence imaging were performed, as described above.

For serum protein studies, 4T1 cells were grown to near confluence in 96 well plates as described above. Prior to the beginning of each experiment, all wells were aspirated and 100 µL of Cy5 conjugated SA-E (20 µM) was added to each well in the cell culture media with or without 10% FBS. SA-E containing growth media were preincubated for 30 min to ensure complete LP binding. Then, the plate was incubated at room temperature for 30 min and all wells were washed 3x with 150 µL sterile PBS (10 mM, pH 7.4). 100 µL of cell growth media, either with or without FBS as appropriate, were added to each well and the plate was returned to the incubator for 1 hour. To stain cell nuclei, a 1:5000 dilution of Hoechst stain was made in serum free media and added to each well. The plate was incubated for 5 min and fluorescence images were taken using a Leica Thunder DMi8 fluorescent microscope using LAS X software.

For SR-B1 studies, an equal number of wells in a black walled, glass bottom 96-well plate were seeded with either wild type or SR-B1-/- TRAMP-C2 cells and grown to near confluency, as above. The Cy5 conjugated SA-E was diluted in 10% FBS containing DMEM and incubated at room temperature for 30 min. All media from the wells was aspirated. Four well of each cell type received 100 μL aliquots with SA-E (20 μM). The plate was incubated for 30 min, as above. The wells were washed with sterile PBS, as above, media was added, and the plate was returned to the incubator for 1 hour. Finally, Hoechst staining and fluorescence imaging were performed, as described above.

Mouse tumor models. All experiments were approved by Oregon Health and Science University (OHSU) Institutional Animal Care and Use Committee (IACUC) (TR01_IP00000674) and conformed to the guidelines set by United States Animal Welfare Act and the National Institutes of Health. Mice were aged between 3-8 months and 20-30 g in weight and were housed in specific pathogen free cages. Human and rat cells were injected into either nude mice (The Jackson Laboratory, 002019) or NSG mice (The Jackson Laboratory, 005557). 4T1 cells were injected into Balb/c mice (The Jackson Laboratory, 000651). LLC, MC38 and TRAMP-C2 were injected into C57Bl/6J mice (The Jackson Laboratory, 000664). Apc^{min} and MMTV-PyMT mice were purchased from the Jackson Laboratory (002020 and 002374). ApoA1 knockout mice were purchased from the Jackson Laboratory (002055). Patient derived xenografts were generated by injecting the patient derived cancer cells subcutaneously in NSG mice.

Tumor accumulation in mice. For the following experiments, mice were injected intravenously (IV) with 100 μL of ICG conjugated SA-E (0.5 mM) or free ICG (0.5 mM). For tumor accumulation studies, cells ($0.5–1\times10^6$ cells) were injected subcutaneously (HCT-116, A375, TRAMP-C2, MC38, LLC, RG2, PDX cell lines), intradermally (A375 cells), or into the fat pad (4T1 and MCF-7 cells). Cells were then allowed to grow into tumor mass of 0.5-1 cm, typically 1-3 weeks. After probe injections, mice were imaged using the IVIS Spectrum (PerkinElmer) with excitation and emission wavelengths of 745 and 820 nm, respectively, at the specified time points. For MMTV mice experiments, mice were injected IV weekly with SA-E (100 μL, 0.5 mM) at age of 14 weeks and imaged 2 days later in the IVIS. For Apc^{min} mice experiments, mice were aged to 4 months to allow intestinal tumors to form. SA-E was injected IV (100 μL, 0.5 mM), 2 days later the intestinal tissue was harvested, washed and analyzed in the IVIS for ICG. For the ApoA1

experiments, ApoA1 knockout or wild-type mice were subcutaneously injected with syngeneic MC38 cancer cells. Tumors were allowed to form to 0.5-1 cm and then injected IV with SA-E (100 μL, 0.5 mM). 2 days later the mice were euthanized and tumors were excised and analyzed in the IVIS for ICG. Living Image (PerkinElmer) software was used for all analyses.

Blood circulation in mice. For blood circulation experiments, wild type mice were injected with 100 μL of ICG conjugated SA-E or free ICG (0.5 mM). Then, blood was drawn via the saphenous vein or retroorbitally at different time points between right after injection and 1 day. 2 μL of blood were diluted into 98 μL of PBS (10 mM, pH 7.4) and ICG fluorescence was measured using a microplate reader (TECAN Spark 20M) at excitation and emission wavelengths of 745 and 820 nm, respectively.

Biodistribution in mice. For biodistribution studies mice containing 4T1 tumors were injected IV with 100 μL of ICG conjugated SA-E (0.5 mM). 2 days after SA-E injection, the mice were euthanized and tumors and organs were excised and analyzed in the IVIS for ICG. Living Image (PerkinElmer) software was used for analysis.

Toxicity in mice. Wild type mice were injected IV with ICG conjugated SA-E at 4 times the dose used for imaging, 100 μL of 2 mM solution. 1 day later, blood was removed via cardiac puncture, placed into an EDTA tube and then centrifuged at 1500g for 10 min, then 2500g for 10 min to obtain plasma. The plasma was analyzed for Aspartate Aminotransferase activity (AST) (Abcam, AB105135) and creatinine (Crystal Chem, 80350) following the manufacturers protocol. For complete blood counts, whole blood (10 μL) was mixed with 2 mM EDTA (10 μL) and analyzed using the HemaVet 950S (Drew Scientific).

Flow cytometry. Nude mice were given RG2-mCherry cells subcutaneously and allowed to grown to be 0.5-1 cm. Mice were then injected intravenously with the Cy5 labeled SA-E (100 μL, 0.5 mM). 2 days later, tumors were extracted, minced and dissociated using 1 mg/mL solution collagenase/dispase (Roche, 10269638001 and 11097113001) for 45 min at 37 °C. The solution was broken down with pipetting and filtered through a 70 μm filter. The single cell solution from suspended in sterile PBS (10 mM, pH 7.4) and then incubated with 1:50 dilution of AlexaFluor 488 Rat Anti-Mouse CD45 antibody (BD Pharminogen, 567377) for 45 min at room temperature. Finally, the cells were pelleted and washed and incubated with 5 μM Calcein Blue, AM (Invitrogen, C1429) for 20 min. The cells were then analyzed in BD FACSymphony in the DAPI

channel (355nm laser, 450/50 filter), FITC channel (488 nm laser, 515/30 filter), Cy3 channel (561 nm laser, 586/15 filter), and Cy5 channel (628 nm laser, 670/30 filter). Cells in culture were used to establish size and mCherry intensity. Tumors from mice that did not receive any SA-E injection and unstained cells were used as controls for gating of SA-E and CD45. Finally, three experimental mice were analyzed in all channels using the gating established from the controls. Gating was performed in FlowJo software.

Rat models. The care and use of animals were approved by the Institutional Animal Care and Use Committee and were supervised by the OHSU Department of Comparative Medicine (DCM) (protocol IP00000843). Female nude (rnu/rnu) rats (150–250 g) were purchased from Charles River Laboratories and female Long Evans rats (200-300g) were purchased from Charles River Laboratories by OHSU DCM. Rats were anesthetized using 3% isoflurane and a 2-mm diameter hole drilled in the skull using a 27-gauge needle) in a stereotactic frame (David Kopf Instruments; Tujunga, CA). Cancer cells (10^6 cells/10 μL, >90% viability) were injected at a rate of 1 μL/min. Human GBM39 tumor cells and rat RG2 cells or mCherry+ RG2 cells were implanted into the right caudate nucleus (bregma= 0; lateral 0.31 cm; vertical - 0.65 cm).

MRI of rat tumors. MRI was performed to confirm tumor growth prior to administration of SA-E using a horizontal bore 11.75 T magnet (Bruker Scientific Instruments, Billerica MA) maintained by OHSU Advanced Imaging Research Center (AIRC). Animals were imaged 8-35 days after tumor implantation, dependent on tumor type. Under intraperitoneal dexmedetomidine (Zoetis, 0.5 mg/kg) and ketamine (Zoetis, 60 mg/kg) sedation, the lateral caudal vein was catheterized and the animal was securely placed in a Plexiglas holder and positioned in the small animal MRI. T1 (Fat saturated 2D Spine Echo [SE], TR 160, TE 1.654), T2 (2D SE, TR 4020.62, TE 23.64) and T2* (2D Gradient Echo, TR 430.25, TE 6.656, FA 30) sequences were obtained prior to a dose of 50 μmol/kg of Omniscan via tail vein catheter followed by a ~0.25 mL saline flush. A post-contrast T1 scan was repeated 5 minutes following administration of Omniscan.

IVIS and fluorescence imaging of rat tumors. After confirmation of the formation of RG2 or GBM39 tumors, ICG conjugated SA-E solution (1 mL, 0.5 mM) was delivered via tail vein catheter, followed by a ~0.25 mL saline flush, prior to anesthetic reversal with intraperitoneal atipamezole HCl (Antisedan, 1.0 mg/kg). For IVIS imaging of rat tumors, animals were euthanized with euthasol (Virbac) via intracardiac injection under isoflurane anesthetization 2 days after SA-

E administration. Brain, heart, lung, liver, spleen and kidney were harvested and stored in a PBS solution until IVIS imaging. Tissues were first imaged in the IVIS for ICG signal. Then, whole-mount brain sections were imaged under IVIS for ICG signal of SA-E and mCherry signal of RG2 cells. For fluorescence imaging of brain sections, brain tissue was flash frozen and stored at -80 °C. Tissue was then sectioned in a cryostat at 20 μm, then fixed in 4% formaldehyde for 10 min. Tissue sections were counterstained with Hoechst and imaged on a Leica Thunder Wide Field Fluorescent Microscope with a 40X objective.

Cytotoxicity of SA-E-MMAE. To assess the cytotoxicity of SA-E-MMAE and free MMAE, 4T1 cells and RG2 cells were seeded in 96-well plates at a density of 5×10^3 cells per well in 100 μL of RPMI (10% FBS). The plates were then incubated at 37 °C under 5% CO_2 for 1 day prior to the addition of SA-E-MMAE or free MMAE, resulting in final drug concentrations ranging from 0 to 10 μM for SA-E-MMAE and 0 to 0.05 μM for MMAE. Plates were further incubated at 37 °C under 5% CO_2 for 3 days. To evaluate cellular viabilities, the RPMI media in each well was replaced with fresh RPMI containing 10% MTS reagent. Subsequently, plates were incubated at 37 °C under 5% CO_2 for 2 hours before measuring the MTS absorbance at 490 nm using a microplate reader (TECAN Spark 20M).

Antitumor effect of SA-E-MMAE. Mice were given 5×10^5 cells injected into either the fat pad (4T1 in Balb/c mice) or subcutaneously (RG2 in nude mice). Mice were then treated IV with the free MMAE (0.1 or 0.3 mg/kg), SA-E-MMAE (0.3, 0.6, or 1 mg/kg) or PBS (10 mM, pH 7.4). 5 doses were given at 2, 4, 7, 9, and 11 days after tumor implantation. For 0.3 mg/kg dose of free MMAE, drug was administered 3 times as a significant weight loss was observed after the third injection. Mouse weight was monitored throughout the study. Tumor size was measured in two directions with a caliper 2-3 times per week rounded to the nearest tenth of a mm. Volume was calculated as a basic sphere of $4/3\pi r^3$.

References

1. Levin, A. *et al.* Biomimetic peptide self-assembly for functional materials. *Nat. Rev. Chem.* **4**, 615–634 (2020).

2. Vicente-Garcia, C. & Colomer, I. Lipopeptides as tools in catalysis, supramolecular, materials and medicinal chemistry. *Nat. Rev. Chem.* **7**, 710–731 (2023).

3. Zhao, X. *et al.* Molecular self-assembly and applications of designer peptide amphiphiles. *Chem. Soc. Rev.* **39**, 3480 (2010).

4. Versluis, F., Marsden, H. R. & Kros, A. Power struggles in peptide-amphiphile nanostructures. *Chem. Soc. Rev.* **39**, 3434 (2010).

5. Dasgupta, A. & Das, D. Designer Peptide Amphiphiles: Self-Assembly to Applications. *Langmuir* **35**, 10704–10724 (2019).

6. Zhang, S. Fabrication of novel biomaterials through molecular self-assembly. *Nat. Biotechnol.* **21**, 1171–1178 (2003).

7. Mikhalevich, V., Craciun, I., Kyropoulou, M., Palivan, C. G. & Meier, W. Amphiphilic Peptide Self-Assembly: Expansion to Hybrid Materials. *Biomacromolecules* **18**, 3471–3480 (2017).

8. Sinha, N. J., Langenstein, M. G., Pochan, D. J., Kloxin, C. J. & Saven, J. G. Peptide Design and Self-assembly into Targeted Nanostructure and Functional Materials. *Chem. Rev.* **121**, 13915–13935 (2021).

9. Rad-Malekshahi, M., Lempsink, L., Amidi, M., Hennink, W. E. & Mastrobattista, E. Biomedical Applications of Self-Assembling Peptides. *Bioconjug. Chem.* **27**, 3–18 (2016).

10. Hamley, I. W. Biocatalysts Based on Peptide and Peptide Conjugate Nanostructures. *Biomacromolecules* **22**, 1835–1855 (2021).

11. Zhou, Y. *et al.* Molecularly Stimuli-Responsive Self-Assembled Peptide Nanoparticles for Targeted Imaging and Therapy. *ACS Nano* **17**, 8004–8025 (2023).

12. Eskandari, S., Guerin, T., Toth, I. & Stephenson, R. J. Recent advances in self-assembled peptides: Implications for targeted drug delivery and vaccine engineering. *Adv. Drug Deliv. Rev.* **110–111**, 169–187 (2017).

13. Delfi, M. *et al.* Self-assembled peptide and protein nanostructures for anti-cancer therapy: Targeted delivery, stimuli-responsive devices and immunotherapy. *Nano Today* **38**, 101119 (2021).

14. Guo, R.-C. *et al.* Recent progress of therapeutic peptide based nanomaterials: from synthesis

and self-assembly to cancer treatment. *Biomater. Sci.* **8**, 6175–6189 (2020).

15. Acar, H. *et al.* Self-assembling peptide-based building blocks in medical applications. *Adv. Drug Deliv. Rev.* **110**–**111**, 65–79 (2017).

16. Yang, J., An, H.-W. & Wang, H. Self-Assembled Peptide Drug Delivery Systems. *ACS Appl. Bio Mater.* **4**, 24–46 (2021).

17. Trent, A., Marullo, R., Lin, B., Black, M. & Tirrell, M. Structural properties of soluble peptide amphiphile micelles. *Soft Matter* **7**, 9572 (2011).

18. Pitman, M. & Larsen, J. The characterization of self-assembled nanostructures in whole blood. *Anal. Methods* **12**, 2068–2081 (2020).

19. Dube, N. *et al.* Effect of Alkyl Length of Peptide–Polymer Amphiphile on Cargo Encapsulation Stability and Pharmacokinetics of 3-Helix Micelles. *Biomacromolecules* **15**, 2963–2970 (2014).

20. Tsonchev, S., Troisi, A., Schatz, G. C. & Ratner, M. A. On the Structure and Stability of Self-Assembled Zwitterionic Peptide Amphiphiles: A Theoretical Study. *Nano Lett.* **4**, 427–431 (2004).

21. Black, M. *et al.* Self-Assembled Peptide Amphiphile Micelles Containing a Cytotoxic T-Cell Epitope Promote a Protective Immune Response In Vivo. *Adv. Mater.* **24**, 3845–3849 (2012).

22. Missirlis, D., Khant, H. & Tirrell, M. Mechanisms of Peptide Amphiphile Internalization by SJSA-1 Cells in Vitro. *Biochemistry* **48**, 3304–3314 (2009).

23. Monopoli, M. P., Åberg, C., Salvati, A. & Dawson, K. A. Biomolecular coronas provide the biological identity of nanosized materials. *Nat. Nanotechnol.* **7**, 779–786 (2012).

24. Dawson, K. A. & Yan, Y. Current understanding of biological identity at the nanoscale and future prospects. *Nat. Nanotechnol.* **16**, 229–242 (2021).

25. Mahmoudi, M., Landry, M. P., Moore, A. & Coreas, R. The protein corona from nanomedicine to environmental science. *Nat. Rev. Mater.* **8**, 422–438 (2023).

26. Busatto, S. *et al.* Lipoprotein-based drug delivery. *Adv. Drug Deliv. Rev.* **159**, 377–390

(2020).

27. Huang, H., Cruz, W., Chen, J. & Zheng, G. Learning from biology: synthetic lipoproteins for drug delivery. *WIREs Nanomedicine and Nanobiotechnology* **7**, 298–314 (2015).

28. Thaxton, C. S., Rink, J. S., Naha, P. C. & Cormode, D. P. Lipoproteins and lipoprotein mimetics for imaging and drug delivery. *Adv. Drug Deliv. Rev.* **106**, 116–131 (2016).

29. Mulder, W. J. M. *et al.* High-Density Lipoprotein Nanobiologics for Precision Medicine. *Acc. Chem. Res.* **51**, 127–137 (2018).

30. Kuai, R., Li, D., Chen, Y. E., Moon, J. J. & Schwendeman, A. High-Density Lipoproteins: Nature's Multifunctional Nanoparticles. *ACS Nano* **10**, 3015–3041 (2016).

31. Brankatschk, M. & Eaton, S. Lipoprotein Particles Cross the Blood-Brain Barrier in Drosophila. *J. Neurosci.* **30**, 10441–10447 (2010).

32. Benmimoun, B. *et al.* An original infection model identifies host lipoprotein import as a route for blood-brain barrier crossing. *Nat. Commun.* **11**, 6106 (2020).

33. Greenlee, J. D., Subramanian, T., Liu, K. & King, M. R. Rafting Down the Metastatic Cascade: The Role of Lipid Rafts in Cancer Metastasis, Cell Death, and Clinical Outcomes. *Cancer Res.* **81**, 5–17 (2021).

34. Sezgin, E., Levental, I., Mayor, S. & Eggeling, C. The mystery of membrane organization: composition, regulation and roles of lipid rafts. *Nat. Rev. Mol. Cell Biol.* **18**, 361–374 (2017).

35. Sviridov, D., Mukhamedova, N. & Miller, Y. I. Lipid rafts as a therapeutic target: Thematic Review Series: Biology of Lipid Rafts. *J. Lipid Res.* **61**, 687–695 (2020).

36. Li, B., Qin, Y., Yu, X., Xu, X. & Yu, W. Lipid raft involvement in signal transduction in cancer cell survival, cell death and metastasis. *Cell Prolif.* **55**, 13167 (2022).

37. Paramonov, S. E., Jun, H.-W. & Hartgerink, J. D. Self-Assembly of Peptide−Amphiphile Nanofibers: The Roles of Hydrogen Bonding and Amphiphilic Packing. *J. Am. Chem. Soc.* **128**, 7291–7298 (2006).

38. Koda, D., Maruyama, T., Minakuchi, N., Nakashima, K. & Goto, M. Proteinase-mediated

drastic morphological change of peptide–amphiphile to induce supramolecular hydrogelation. *Chem. Commun.* **46**, 979–981 (2010).

39. Zhang, C. *et al.* A Transformable Chimeric Peptide for Cell Encapsulation to Overcome Multidrug Resistance. *Small* **14**, 1703321 (2018).

40. Mundra, V., Peng, Y., Rana, S., Natarajan, A. & Mahato, R. I. Micellar formulation of indocyanine green for phototherapy of melanoma. *J. Control. Release* **220**, 130–140 (2015).

41. Wu, L. *et al.* Hybrid polypeptide micelles loading indocyanine green for tumor imaging and photothermal effect study. *Biomacromolecules* **14**, 3027–3033 (2013).

42. Missirlis, D., Krogstad, D. V. & Tirrell, M. Internalization of p5314-29 peptide amphiphiles and subsequent endosomal disruption results in SJSA-1 cell death. *Mol. Pharm.* **7**, 2173–2184 (2010).

43. Lu, J., Owen, S. C. & Shoichet, M. S. Stability of Self-Assembled Polymeric Micelles in Serum. *Macromolecules* **44**, 6002–6008 (2011).

44. Kratz, F. A clinical update of using albumin as a drug vehicle — A commentary. *J. Control. Release* **190**, 331–336 (2014).

45. Zorzi, A., Middendorp, S. J., Wilbs, J., Deyle, K. & Heinis, C. Acylated heptapeptide binds albumin with high affinity and application as tag furnishes long-acting peptides. *Nat. Commun.* **8**, 16092 (2017).

46. Xu, Y. *et al.* In Situ Albumin-Hitchhiking NIR-II Probes for Accurate Detection of Micrometastases. *Nano Lett.* **23**, 5731–5737 (2023).

47. Sarett, S. M. *et al.* Lipophilic siRNA targets albumin in situ and promotes bioavailability, tumor penetration, and carrier-free gene silencing. *Proc. Natl. Acad. Sci.* **114**, E6490–E6497 (2017).

48. Spada, A., Emami, J., Tuszynski, J. A. & Lavasanifar, A. The Uniqueness of Albumin as a Carrier in Nanodrug Delivery. *Mol. Pharm.* **18**, 1862–1894 (2021).

49. Zhu, G. *et al.* Albumin/vaccine nanocomplexes that assemble in vivo for combination cancer immunotherapy. *Nat. Commun.* **8**, 1954 (2017).

50. Xi, J. *et al.* Long-Circulating Amphiphilic Doxorubicin for Tumor Mitochondria-Specific Targeting. *ACS Appl. Mater. Interfaces* **10**, 43482–43492 (2018).

51. Ren, L. *et al.* Apolipoproteins and cancer. *Cancer Med.* **8**, 7032–7043 (2019).

52. Jang, E., Robert, J., Rohrer, L., von Eckardstein, A. & Lee, W. L. Transendothelial transport of lipoproteins. *Atherosclerosis* **315**, 111–125 (2020).

53. Kraehling, J. R. *et al.* Genome-wide RNAi screen reveals ALK1 mediates LDL uptake and transcytosis in endothelial cells. *Nat. Commun.* **7**, 13516 (2016).

54. Simionescu, M., Popov, D. & Sima, A. Endothelial transcytosis in health and disease. *Cell Tissue Res.* **335**, 27–40 (2009).

55. Conner, S. D. & Schmid, S. L. Regulated portals of entry into the cell. *Nature* **422**, 37–44 (2003).

56. Banushi, B., Joseph, S. R., Lum, B., Lee, J. J. & Simpson, F. Endocytosis in cancer and cancer therapy. *Nat. Rev. Cancer* **23**, 450–473 (2023).

57. Chen, S. *et al.* Enhanced tumour penetration and prolonged circulation in blood of polyzwitterion–drug conjugates with cell-membrane affinity. *Nat. Biomed. Eng.* **5**, 1019–1037 (2021).

58. Chakraborty, A. & Jana, N. R. Clathrin to Lipid Raft-Endocytosis via Controlled Surface Chemistry and Efficient Perinuclear Targeting of Nanoparticle. *J. Phys. Chem. Lett.* **6**, 3688–3697 (2015).

59. Kanatani, I. *et al.* Efficient gene transfer by pullulan–spermine occurs through both clathrin- and raft/caveolae-dependent mechanisms. *J. Control. Release* **116**, 75–82 (2006).

60. Dejonghe, W. *et al.* Disruption of endocytosis through chemical inhibition of clathrin heavy chain function. *Nat. Chem. Biol.* **15**, 641–649 (2019).

61. Tyagi, M., Rusnati, M., Presta, M. & Giacca, M. Internalization of HIV-1 Tat Requires Cell Surface Heparan Sulfate Proteoglycans. *J. Biol. Chem.* **276**, 3254–3261 (2001).

62. Wadia, J. S., Stan, R. V. & Dowdy, S. F. Transducible TAT-HA fusogenic peptide enhances escape of TAT-fusion proteins after lipid raft macropinocytosis. *Nat. Med.* **10**, 310–315

(2004).

63. Campiani, G. *et al.* A Rational Approach to the Design of Selective Substrates and Potent Nontransportable Inhibitors of the Excitatory Amino Acid Transporter EAAC1 (EAAT3). New Glutamate and Aspartate Analogues as Potential Neuroprotective Agents. *J. Med. Chem.* **44**, 2507–2510 (2001).

64. Usama, S. M. *et al.* Role of Albumin in Accumulation and Persistence of Tumor-Seeking Cyanine Dyes. *Bioconjug. Chem.* **31**, 248–259 (2020).

65. Kozarsky, K. F. *et al.* Overexpression of the HDL receptor SR-BI alters plasma HDL and bile cholesterol levels. *Nature* **387**, 414–417 (1997).

66. Ng, K. K., Lovell, J. F. & Zheng, G. Lipoprotein-Inspired Nanoparticles for Cancer Theranostics. *Acc. Chem. Res.* **44**, 1105–1113 (2011).

67. Chaudhary, J., Bower, J. & Corbin, I. R. Lipoprotein Drug Delivery Vehicles for Cancer: Rationale and Reason. *Int. J. Mol. Sci.* **20**, 6327 (2019).

68. Traughber, C. A. *et al.* Uptake of high-density lipoprotein by scavenger receptor class B type 1 is associated with prostate cancer proliferation and tumor progression in mice. *J. Biol. Chem.* **295**, 8252–8261 (2020).

69. Bruns, O. T. *et al.* Real-time magnetic resonance imaging and quantification of lipoprotein metabolism in vivo using nanocrystals. *Nat. Nanotechnol.* **4**, 193–201 (2009).

70. Attalla, S., Taifour, T., Bui, T. & Muller, W. Insights from transgenic mouse models of PyMT-induced breast cancer: recapitulating human breast cancer progression in vivo. *Oncogene* **40**, 475–491 (2021).

71. Moser, A. R. *et al.* ApcMin: A mouse model for intestinal and mammary tumorigenesis. *Eur. J. Cancer* **31**, 1061–1064 (1995).

72. Bryant, P. *et al.* In Vitro and In Vivo Evaluation of Cysteine Rebridged Trastuzumab–MMAE Antibody Drug Conjugates with Defined Drug-to-Antibody Ratios. *Mol. Pharm.* **12**, 1872–1879 (2015).

73. Hingorani, D. V. *et al.* Monomethyl auristatin antibody and peptide drug conjugates for

trimodal cancer chemo-radio-immunotherapy. *Nat. Commun.* **13**, 3869 (2022).

74. Mo, Z.-C., Ren, K., Liu, X., Tang, Z.-L. & Yi, G.-H. A high-density lipoprotein-mediated drug delivery system. *Adv. Drug Deliv. Rev.* **106**, 132–147 (2016).

75. Zhu, C. & Xia, Y. Biomimetics: reconstitution of low-density lipoprotein for targeted drug delivery and related theranostic applications. *Chem. Soc. Rev.* **46**, 7668–7682 (2017).

76. Wasan, K. M., Brocks, D. R., Lee, S. D., Sachs-Barrable, K. & Thornton, S. J. Impact of lipoproteins on the biological activity and disposition of hydrophobic drugs: implications for drug discovery. *Nat. Rev. Drug Discov.* **7**, 84–99 (2008).

77. Sobot, D. *et al.* Conjugation of squalene to gemcitabine as unique approach exploiting endogenous lipoproteins for drug delivery. *Nat. Commun.* **8**, 15678 (2017).

78. Coppens, E. *et al.* Gemcitabine lipid prodrug nanoparticles: Switching the lipid moiety and changing the fate in the bloodstream. *Int. J. Pharm.* **609**, 121076 (2021).

79. Yesylevskyy, S. O., Ramseyer, C., Savenko, M., Mura, S. & Couvreur, P. Low-Density Lipoproteins and Human Serum Albumin as Carriers of Squalenoylated Drugs: Insights from Molecular Simulations. *Mol. Pharm.* **15**, 585–591 (2018).

80. Babič, A. *et al.* 5-Aminolevulinic Acid-Squalene Nanoassemblies for Tumor Photodetection and Therapy: In Vitro Studies. *Nanoscale Res. Lett.* **13**, 10 (2018).

Acknowledgements

Authors thank Drs. Melissa Wong, Jonathan D. Smith, and Jann N. Sarkaria for providing MC38, TRAMP-C2 (wild type and SR-B1-/-), and PDX GBM39 glioblastoma cells, respectively. Authors thank Randall J. Armstrong for his help with FPLC measurements. Mass spectrometric analysis was performed by the OHSU Proteomics Shared Resource with partial support from NIH core grants P30EY010572, P30CA069533 and OHSU Emerging Technology Fund. Author Ramon F. Barajas Jr is supported by NIH NCI 1K08CA237809 and L30 CA220897. Authors Leslie Muldoon and Ramon F Barajas Jr. are supported by Jonathan D + Mark C. Lewis Foundation. This project

was supported by funding from the Cancer Early Detection Advanced Research (CEDAR) center at the Oregon Health & Science University's Knight Cancer Institute.

Author contributions

A.Y. designed the PAs. J.M.F. and A.Y. designed the study. L.L.M. and R.F.B. designed rat studies. B.P.B. provided insights on the concept. M.D. and L.X. performed PA conjugations and purification. M.S. performed fluorescence and FPLC experiments. M.S. and F.G. performed sample preparation for MS measurements. S.S. performed TEM imaging. I.D. and S.R. designed and conducted MD simulations. J.M.F., S.D., B.R.K., and K.B. performed cellular uptake and transcytosis experiments. J.M.F., A.Q., S.D., and X.Y. performed mouse studies. J.M.F. and S.H. performed rat studies. L.X. performed cytotoxicity studies. J.M.F. and A.Y. wrote the manuscript with input from all authors.

Competing interests

A.Y., J.M.F., and B.P.B submitted a patent application (PCT/US2022/073964) on the early findings of this study. The other authors declare no competing interests.